

## Multiparameter entanglement in femtosecond parametric down-conversion

Mete Atatüre,<sup>1</sup> Giovanni Di Giuseppe,<sup>2</sup> Matthew D. Shaw,<sup>2</sup> Alexander V. Sergienko,<sup>1,2</sup> Bahaa E. A. Saleh,<sup>2</sup> and Malvin C. Teich,<sup>1,2</sup>

<sup>1</sup>*Quantum Imaging Laboratory, Department of Physics, Boston University, 8 Saint Mary's Street, Boston, Massachusetts 02215*

<sup>2</sup>*Quantum Imaging Laboratory, Department of Electrical and Computer Engineering, Boston University, 8 Saint Mary's Street, Boston, Massachusetts 02215*

(Received 14 August 2001; published 11 January 2002)

A theory of spontaneous parametric down-conversion, which gives rise to a quantum state that is entangled in multiple parameters, such as three-dimensional wave vector and polarization, allows us to understand the unusual characteristics of fourth-order quantum interference in many experiments, including ultrafast type-II parametric down-conversion, the specific example illustrated in this paper. The comprehensive approach provided here permits the engineering of quantum states suitable for quantum-information schemes and quantum technologies.

DOI: 10.1103/PhysRevA.65.023808

PACS number(s): 42.50.Dv, 03.67.-a, 42.65.Re, 42.65.Ky

### INTRODUCTION

Entanglement [1] is, undoubtedly, one of the most fascinating features of quantum mechanics. Spontaneous parametric down-conversion (SPDC) [2], a nonlinear optical phenomenon, has been one of the most widely used sources of entangled quantum states. In this process, pairs of photons are generated in a state that can be entangled in frequency, momentum, and polarization when a laser beam illuminates a nonlinear optical crystal. The experimental arrangement for producing entangled photon pairs is simple both in conception and in execution.

Ironically, a significant number of experimental efforts designed to verify the nonseparability of entangled states, the hallmark of entanglement, are carried out in the context of models that fail to access the overall relevant Hilbert space, but rather are restricted to only a *single* kind of entanglement, such as entanglement in energy [3], momentum [4], or polarization [5]. Inconsistencies in the analysis of down-conversion quantum-interference experiments can emerge under such circumstances, as highlighted by the failure of the conventional theory [6] of ultrafast parametric down-conversion to characterize quantum-interference experiments [7].

In this paper we present a quantum-mechanical analysis of entangled-photon state generation via type-II SPDC, considering *simultaneous* entanglement in three-dimensional wave vector and polarization at the generation, propagation, and detection stages. As one specific example of the applicability of this approach, we use it to describe both new and previously obtained [7] results of SPDC experiments with a femtosecond pump. Our analysis confirms that the inconsistencies between existing theoretical models and the observed data in femtosecond down-conversion experiments can indeed be attributed to a failure of considering the full Hilbert space spanned by the simultaneously entangled quantum variables. Femtosecond SPDC models have heretofore ignored transverse wave vector components and have thereby not accounted for the previously demonstrated angular spread [8] of the down-converted light. The approach presented here is suitable for type-I as well as type-II, sponta-

neous parametric down-conversion in the paraxial approximation, which is valid for the great preponderance of experimental SPDC efforts to date.

Our study leads to a deeper physical understanding of hyperentangled-photon states and, concomitantly, provides a route for engineering these states for specific applications, including quantum-information processing.

### HYPERENTANGLED-STATE GENERATION

With this motivation we present a multidimensional analysis of the entangled-photon state generated via SPDC. To admit a broad range of possible experimental schemes we consider, in turn, three general and fundamentally distinct stages in any experimental apparatus: the generation, propagation, and detection of the quantum state [9].

We begin with generation. By virtue of the weak nonlinear interaction, we consider the state generated within the confines of the first-order time-dependent perturbation theory

$$|\Psi^{(2)}\rangle \sim \frac{i}{\hbar} \int_{t_0}^t dt' \hat{H}_{\text{int}}(t') |0\rangle. \quad (1)$$

Here  $\hat{H}_{\text{int}}(t')$  is the interaction Hamiltonian,  $(t_0, t)$  is the duration of the interaction, and  $|0\rangle$  is the initial vacuum state. The interaction Hamiltonian governing this phenomenon is [10]

$$\hat{H}_{\text{int}}(t') \sim \chi^{(2)} \int_V d\mathbf{r} \hat{E}_p^{(+)}(\mathbf{r}, t') \hat{E}_o^{(-)}(\mathbf{r}, t') \hat{E}_e^{(-)}(\mathbf{r}, t') + \text{H.c.}, \quad (2)$$

where  $\chi^{(2)}$  is the second-order susceptibility and  $V$  is the volume of the nonlinear medium in which the interaction takes place. The symbol  $\hat{E}_j^{(\pm)}(\mathbf{r}, t')$  represents the positive- (negative-) frequency portion of the  $j$ th electric-field operator, with the subscript  $j$  representing the pump ( $p$ ), ordinary ( $o$ ), and extraordinary ( $e$ ) waves at position  $\mathbf{r}$  and time  $t'$ , and H.c. stands for Hermitian conjugate. In the paraxial approximation, the polarization of each photon ( $o, e$ ) may be

assumed to be independent of frequency and wave vector (the dependence at large angles is considered in Ref. [11]). Due to the high intensity of the pump field we take the coherent-state laser beam to be classical, with an arbitrary spatiotemporal profile given by

$$E_p(\mathbf{r}, t) = \int d\mathbf{k}_p \tilde{E}_p(\mathbf{k}_p) e^{i\mathbf{k}_p \cdot \mathbf{r}} e^{-i\omega_p(\mathbf{k}_p)t}, \quad (3)$$

where  $\tilde{E}_p(\mathbf{k}_p)$  is the complex-amplitude profile of the field as a function of the wave vector  $\mathbf{k}_p$ .

In contrast with previous models we consider the wavevector to be three dimensional, with a transverse wavevector  $\mathbf{q}_p$  and frequency  $\omega_p$ , so that Eq. (3) takes the form

$$E_p(\mathbf{r}, t) = \int d\mathbf{q}_p d\omega_p \tilde{E}_p(\mathbf{q}_p; \omega_p) e^{i\kappa_p z} e^{i\mathbf{q}_p \cdot \mathbf{x}} e^{-i\omega_p t}, \quad (4)$$

where  $\mathbf{x}$  spans the transverse plane perpendicular to the propagation direction  $z$ . In a similar way the signal and idler fields can be expressed in terms of the quantum-mechanical creation operators  $\hat{a}^\dagger(\mathbf{q}, \omega)$  for the  $(\mathbf{q}, \omega)$  modes as

$$\hat{E}_j^{(-)}(\mathbf{r}, t) = \int d\mathbf{q}_j d\omega_j e^{-i\kappa_j z} e^{-i\mathbf{q}_j \cdot \mathbf{x}} e^{i\omega_j t} \hat{a}_j^\dagger(\mathbf{q}_j, \omega_j), \quad (5)$$

where the subscript  $j = o, e$ . The longitudinal component of  $\mathbf{k}$ , denoted  $\kappa$ , can be written in terms of the  $(\mathbf{q}, \omega)$  pair as [9]

$$\kappa = \left\{ \left[ \frac{n_e(\omega, \theta)}{c} \right]^2 - |\mathbf{q}|^2 \right\}^{1/2}, \quad (6)$$

where  $\theta$  is the angle between  $\mathbf{k}$  and the optical axis of the nonlinear crystal,  $n_e(\omega, \theta)$  is the extraordinary index of refraction in the nonlinear medium, and  $c$  is the speed of light in vacuum. Note that the extraordinary refractive index,  $n_e(\omega, \theta)$ , in Eq. (6) should be replaced by the ordinary refractive index,  $n_o(\omega)$ , when calculating  $\kappa$  for ordinary waves.

Substituting Eqs. (4) and (5) into Eqs. (1) and (2) yields the wave function at the output of the nonlinear crystal

$$|\Psi^{(2)}\rangle \sim \int d\mathbf{q}_o d\mathbf{q}_e d\omega_o d\omega_e \Phi(\mathbf{q}_o, \mathbf{q}_e; \omega_o, \omega_e) \times \hat{a}_e^\dagger(\mathbf{q}_o, \omega_o) \hat{a}_e^\dagger(\mathbf{q}_e, \omega_e) |0\rangle, \quad (7)$$

with

$$\Phi(\mathbf{q}_o, \mathbf{q}_e; \omega_o, \omega_e) = \tilde{E}_p(\mathbf{q}_o + \mathbf{q}_e; \omega_o + \omega_e) \times L \operatorname{sinc}\left(\frac{L\Delta}{2}\right) e^{-iL\Delta/2}. \quad (8)$$

Here  $\Delta = \kappa_p - \kappa_o - \kappa_e$ , where  $\kappa_j$  ( $j = p, o, e$ ) is related to the indices  $(\mathbf{q}_j, \omega_j)$  via relations similar to Eq. (6). The nonsepa-

rability of the function  $\Phi(\mathbf{q}_o, \mathbf{q}_e; \omega_o, \omega_e)$  in Eqs. (7) and (8), recalling Eq. (6), is the hallmark of *simultaneous* multiparameter entanglement.

### HYPERENTANGLED-STATE PROPAGATION

Propagation between the planes of generation and detection is characterized by the classical transfer function of the optical system. The biphoton probability amplitude at the space-time coordinates  $(\mathbf{x}_A, t_A)$  and  $(\mathbf{x}_B, t_B)$ , where detection will take place, is defined by [10]

$$A(\mathbf{x}_A, \mathbf{x}_B; t_A, t_B) = \langle 0 | \hat{E}_A^{(+)}(\mathbf{x}_A, t_A) \hat{E}_B^{(+)}(\mathbf{x}_B, t_B) | \Psi^{(2)} \rangle. \quad (9)$$

The explicit forms of the quantum fields present at the detection locations are represented by

$$\begin{aligned} \hat{E}_A^{(+)}(\mathbf{x}_A, t_A) &= \int d\mathbf{q} d\omega e^{-i\omega t_A} [\mathcal{H}_{Ae}(\mathbf{x}_A, \mathbf{q}; \omega) \hat{a}_e(\mathbf{q}, \omega) \\ &\quad + \mathcal{H}_{Ao}(\mathbf{x}_A, \mathbf{q}; \omega) \hat{a}_o(\mathbf{q}, \omega)], \\ \hat{E}_B^{(+)}(\mathbf{x}_B, t_B) &= \int d\mathbf{q} d\omega e^{-i\omega t_B} [\mathcal{H}_{Be}(\mathbf{x}_B, \mathbf{q}; \omega) \hat{a}_e(\mathbf{q}, \omega) \\ &\quad + \mathcal{H}_{Bo}(\mathbf{x}_B, \mathbf{q}; \omega) \hat{a}_o(\mathbf{q}, \omega)], \end{aligned} \quad (10)$$

where the transfer function  $\mathcal{H}_{ij}$  ( $i = A, B$  and  $j = e, o$ ) describes the propagation of a  $(\mathbf{q}, \omega)$  mode from the nonlinear-crystal output plane to the detection plane. Substituting Eqs. (7) and (10) into Eq. (9) yields a general form for the biphoton probability amplitude,

$$\begin{aligned} A(\mathbf{x}_A, \mathbf{x}_B; t_A, t_B) &= \int d\mathbf{q}_o d\mathbf{q}_e d\omega_o d\omega_e \Phi(\mathbf{q}_o, \mathbf{q}_e; \omega_o, \omega_e) \\ &\quad \times [\mathcal{H}_{Ae}(\mathbf{x}_A, \mathbf{q}_e; \omega_e) \mathcal{H}_{Bo}(\mathbf{x}_B, \mathbf{q}_o; \omega_o) \\ &\quad \times \exp\{-i(\omega_e t_A + \omega_o t_B)\}] \\ &\quad + \mathcal{H}_{Ao}(\mathbf{x}_A, \mathbf{q}_o; \omega_o) \mathcal{H}_{Be}(\mathbf{x}_B, \mathbf{q}_e; \omega_e) \\ &\quad \times \exp\{-i(\omega_o t_A + \omega_e t_B)\}]. \end{aligned} \quad (11)$$

This function can be separated into polarization-dependent and -independent terms, as necessary, for any particular configuration. By choosing explicit forms of the functions  $\mathcal{H}_{Ae}$ ,  $\mathcal{H}_{Ao}$ ,  $\mathcal{H}_{Be}$ , and  $\mathcal{H}_{Bo}$ , the overall biphoton probability amplitude can be sculpted as desired.

### HYPERENTANGLED-STATE DETECTION

The formulation of the detection process depends on the scheme to be used. Slow detectors, for example, impart temporal integration while finite area detectors impart spatial integration. Quantum-interference experiments typically make use of just such detectors. Under these conditions, the

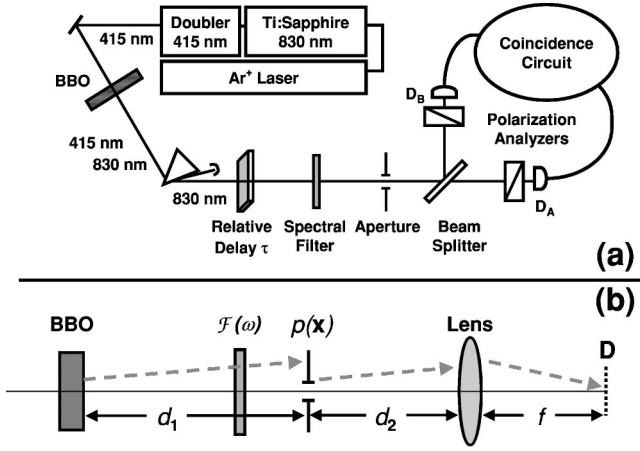


FIG. 1. (a) Schematic of the experimental setup for observation of quantum interference using femtosecond SPDC. (b) Details of the path from the crystal output plane to the detector input plane.

coincidence count rate  $R$  is readily expressed in terms of the biphoton probability amplitude

$$R = \int d\mathbf{x}_A d\mathbf{x}_B dt_A dt_B |A(\mathbf{x}_A, \mathbf{x}_B; t_A, t_B)|^2. \quad (12)$$

#### EXAMPLE: QUANTUM INTERFERENCE IN ULTRAFAST SPDC

We now consider a particular example that demonstrates the validity of our analysis: an ultrafast polarization quantum-interference experiment of the form illustrated in Fig. 1(a). Details of the experimental arrangement and protocol can be found in an earlier work [7]; in the analysis offered there we made use of a phenomenological model that considered a collection of contributions from different regions in the nonlinear crystal that, in the absence of a full quantum-mechanical model, were conjectured to be independent and distinguishable. With the help of the general spatiotemporal quantum-mechanical approach developed here, we are now in a position to provide a complete analysis of those data along with new data in which filtering was used (presented in Figs. 2 and 3, respectively).

For the polarization-interferometer arrangement illustrated in Fig. 1(a), in the presence of a polarization-dependent relative temporal delay  $\tau$ , Eq. (10) can be conveniently separated into polarization-dependent and -independent terms via the relation

$$\mathcal{H}_{ij}(\mathbf{x}_i, \mathbf{q}; \omega) = (\mathbf{e}_i \cdot \mathbf{e}_j) e^{-i\omega\tau\delta_{ej}} H(\mathbf{x}_i, \mathbf{q}; \omega), \quad (13)$$

where  $i = A, B$  and  $j = e, o$ . The symbol  $\delta_{ej}$  is the Kronecker delta so that  $\delta_{ee} = 1$  and  $\delta_{eo} = 0$ . The unit vector  $\mathbf{e}_i$  describes the orientation of the polarization analyzers in the experimental apparatus [see Fig. 1(a)], while  $\mathbf{e}_j$  is the unit vector that describes the polarization of the down-converted photons; the function  $H(\mathbf{x}_i, \mathbf{q}; \omega)$  is the transfer function of the polarization-independent elements of the system, such as free space, filters, apertures, and lenses, as illustrated in Fig.

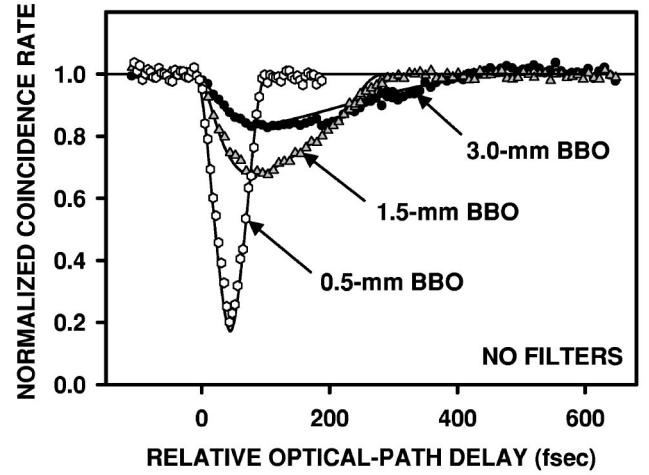


FIG. 2. Experimental (symbols) and theoretical (solid curves) results for the normalized coincidence rate for BBO crystals of three different lengths (hexagons: 0.5 mm; triangles: 1.5 mm; circles: 3.0 mm) as a function of the relative optical-path delay  $\tau$ . As the crystal length increases the fringe visibility diminishes substantially and a dramatic asymmetry emerges. No free parameters are used to fit the data.

1(b). The paraxial approximation satisfactorily describes our experiments so that the explicit form of  $H$  in Fig. 1(b) becomes

$$H(\mathbf{x}, \mathbf{q}; \omega) = \left[ \exp\left\{i\frac{\omega}{c}(d_1 + d_2 + f)\right\} \exp\left\{-i\frac{\omega|\mathbf{x}|^2}{2cf}\left(\frac{d_2}{f} - 1\right)\right\} \right] \times \exp\left\{-i\frac{d_1c}{2\omega}|\mathbf{q}|\right\} \tilde{P}\left(\frac{\omega}{cf}\mathbf{x} - \mathbf{q}\right) \mathcal{F}(\omega), \quad (14)$$

where  $d_1$ ,  $d_2$ , and  $f$  (focal length of the lens) are indicated,  $\tilde{P}$  is the aperture function  $p(\mathbf{x})$  in the Fourier domain, and  $\mathcal{F}(\omega)$  is the spectral filter function.

Using Eqs. (13) and (14) in Eq. (11), the biphoton probability amplitude for the arrangement shown in Fig. 1(a) therefore becomes

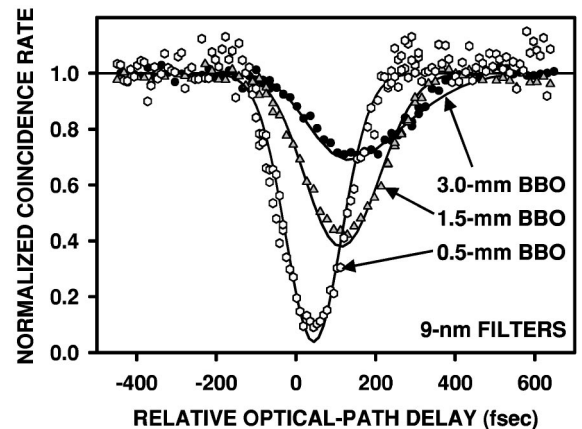


FIG. 3. Plots similar to those in Fig. 2 in the presence of an interference filter of 9-nm bandwidth. The patterns are symmetrized.

$$A(\mathbf{x}_A, \mathbf{x}_B; t_A, t_B) = \int d\mathbf{q}_o d\mathbf{q}_e d\omega_o d\omega_e \Phi(\mathbf{q}_o, \mathbf{q}_e; \omega_o, \omega_e) e^{-i\omega_e \tau} [(\mathbf{e}_A \cdot \mathbf{e}_e)(\mathbf{e}_B \cdot \mathbf{e}_o) H(\mathbf{x}_A, \mathbf{q}_e; \omega_e) H(\mathbf{x}_B, \mathbf{q}_o; \omega_o) e^{-i(\omega_e t_A + \omega_o t_B)} + (\mathbf{e}_A \cdot \mathbf{e}_o)(\mathbf{e}_B \cdot \mathbf{e}_e) H(\mathbf{x}_A, \mathbf{q}_o; \omega_o) H(\mathbf{x}_B, \mathbf{q}_e; \omega_e) e^{-i(\omega_o t_A + \omega_e t_B)}]. \quad (15)$$

Using this form for the biphoton probability amplitude in Eq. (12) yields the coincidence-count rate as a function of the polarization-dependent temporal delay  $\tau$ .

### DISCUSSION

Figure 2 displays the observed normalized coincidence rates (fourth-order quantum-interference patterns) for 0.5-, 1.5-, and 3.0-mm  $\beta$ -barium borate (BBO) crystals (symbols), in the absence of spectral filtering, along with the expected theoretical curves (solid), as a function of relative optical-path delay  $\tau$ . We have treated the pump as a finite-bandwidth pulsed plane wave, an assumption that is valid in our experimental setup. The asymmetry of the observed interference pattern clearly increases with increasing crystal thickness.

Figure 3 provides a set of data collected in a similar fashion, but this time observed in the presence of a narrowband (9 nm) spectral filter  $\mathcal{F}(\omega)$ , as illustrated in Fig. 1(b). The most dramatic effect of including the filter is the symmetrization of the quantum-interference patterns. Since  $\mathbf{q}$  and  $\omega$  are intrinsically linked by Eq. (8), the imposition of spectral filtering restricts the allowable transverse wave vector spread. Spectral and spatial filtering, therefore, have similar effects for non-cross-spectrally pure light, such as that generated in SPDC [8].

The increasing asymmetry and loss of visibility in Figs. 2

and 3 are observed with increasing crystal thickness, as the extent of the  $(\mathbf{q}, \omega)$  modes overlap less in space at the detection plane. This decreased overlap leads to increased distinguishability. This distinguishability is similar in nature to the *spectral* distinguishability in the one-dimensional model discussed in Ref. [6]. The physical origin of this behavior resides in the angle dependence (hence  $\mathbf{q}$  dependence) of the extraordinary refractive index for the down-converted photons [Eq. (6)]. Although the phase-matching condition between the pump and the down-converted photon pairs encompasses a large range of  $(\mathbf{q}, \omega)$  modes at the source, the combination of free-space propagation and the small acceptance angle of the optical system leads to diffraction of the SPDC beams, which, in turn, results in increased overlap and, therefore, a decrease in distinguishability. Indeed, when the aperture size becomes sufficiently small, the observed quantum-interference patterns ultimately revert to those calculated using the one-dimensional model that has traditionally been employed.

### ACKNOWLEDGMENTS

This work was supported by the National Science Foundation (NSF) and by the Defense Advanced Research Projects Agency (DARPA).

- 
- [1] E. Schrödinger, *Naturwissenschaften* **23**, 807 (1935); **23**, 823 (1935); **23**, 844 (1935); [translation in *Quantum Theory and Measurement*, edited by J. A. Wheeler and W. H. Zurek (Princeton University Press, Princeton, 1983)].
  - [2] S. E. Harris, M. K. Oshman, and R. L. Byer, *Phys. Rev. Lett.* **18**, 732 (1967); D. Magde and H. Mahr, *ibid.* **18**, 905 (1967).
  - [3] C. K. Hong, Z. Y. Ou, and L. Mandel, *Phys. Rev. Lett.* **59**, 2044 (1987); P. G. Kwiat, A. M. Steinberg, and R. Y. Chiao, *Phys. Rev. A* **47**, R2472 (1993).
  - [4] J. G. Rarity and P. R. Tapster, *Phys. Rev. Lett.* **64**, 2495 (1990).
  - [5] Z. Y. Ou and L. Mandel, *Phys. Rev. Lett.* **61**, 50 (1988); Y. H. Shih and C. O. Alley, *ibid.* **61**, 2921 (1988); Y. H. Shih and A. V. Sergienko, *Phys. Lett. A* **191**, 201 (1994); P. G. Kwiat, K. Mattle, H. Weinfurter, A. Zeilinger, A. V. Sergienko, and Y. H. Shih, *Phys. Rev. Lett.* **75**, 4337 (1995).
  - [6] G. Di Giuseppe, L. Haiberger, F. De Martini, and A. V. Sergienko, *Phys. Rev. A* **56**, R21 (1997); T. E. Keller and M. H. Rubin, *ibid.* **56**, 1534 (1997); W. P. Grice, R. Erdmann, I. A. Walmsley, and D. Branning, *ibid.* **57**, R2289 (1998); J. Peřina, Jr., A. V. Sergienko, B. M. Jost, B. E. A. Saleh, and M. C. Teich, *ibid.* **59**, 2359 (1999).
  - [7] M. Atatüre, A. V. Sergienko, B. M. Jost, B. E. A. Saleh, and M. C. Teich, *Phys. Rev. Lett.* **83**, 1323 (1999).
  - [8] A. Joobeur, B. E. A. Saleh, and M. C. Teich, *Phys. Rev. A* **50**, 3349 (1994); C. H. Monken, P. H. Souto Ribeiro, and S. Pádua, *ibid.* **57**, 3123 (1998); B. E. A. Saleh, A. Joobeur, and M. C. Teich, *ibid.* **57**, 3991 (1998).
  - [9] B. E. A. Saleh, A. F. Abouraddy, A. V. Sergienko, and M. C. Teich, *Phys. Rev. A* **62**, 043816 (2000).
  - [10] B. R. Mollow, *Phys. Rev. A* **8**, 2684 (1973); J. Peřina, Z. Hradil, and B. Jurčo, *Quantum Optics and Fundamentals of Physics* (Kluwer, Boston, 1994).
  - [11] A. Migdall, *J. Opt. Soc. Am. B* **14**, 1093 (1997).